Extrusion-based Additive Manufacturing of Regolith-Filled Shape Memory Vitrimer Composite for Lunar Construction

Kingsley Yeboah Gyabaah[1], Obed Nyavor[2], Bernard Mahoney[1], Maryam Jahan[3], Brett Smith[4], Enrique Jackson[4], Patrick Mensah[1], Guoqiang Li[1,2,*]

[1]Department of Mechanical Engineering, Southern University and A & M College, Baton Rouge, LA 70813, USA

[2]Department of Mechanical & Industrial Engineering, Louisiana State University, Baton Rouge, LA 70803, USA

[3]Department of Chemistry, Southern University and A & M College, Baton Rouge, LA, USA

[4]Mashall Space Flight Center, NASA, 221 Rideout Road, Huntsville, AL 35812, USA

*Corresponding author: lguoqi1@lsu.edu

Abstract

The National Aeronautics and Space Administration (NASA) is visiting the moon again. This time, the objective is to explore establishing a permanent lunar base. To achieve both long-term human habitation on the moon and future deep space travel, it is crucial to make the most of the in-situ resources and build autonomous systems on the moon to support the construction of a lunar habitat. NASA's In-situ Resource Utilization (ISRU) program aims to minimize the need to ship heavy prefabricated structures, reducing cost and enhancing sustainability. Here, we developed an economical extrusion method for printing lunar regolith-based composites using shape memory vitrimer as a binder. A rheological study is conducted to determine the extrudability of the composite with different regolith weight percentages. Several characterizations were conducted on the composites. The as-printed composites exhibited compressive and flexural strengths of **73.32 MPa** and **156.59 MPa**, respectively, and good impact tolerance. The composite maintained **57.92%** of its mechanical properties even after the second crack healing cycle. The composites also exhibit shape fixity ratio of **90.02%** and shape recovery ratio of **83.46%**. The simple synthesis method, sustainability, and good thermomechanical properties make the 3D printed composite an ideal material for lunar construction applications.

Keywords: Extrusion-based 3D Printing, Vitrimer, Shape Memory, Additive Manufacturing, Thixotropy Analysis, Composites

1 Introduction

Extraterrestrial habitation has become a primary extraterrestrial exploration objective for global space agencies, highlighted by NASA's Artemis Project, which aims to return humans to the lunar surface in 2026 [1]. A secondary, long-term goal is the establishment of sustainable habitats to support prolonged scientific exploration and data collection [2]. However, the economic viability of these missions is severely constrained by the high cost of terrestrial exports—currently estimated at $54,000 per kilogram of payload [3, 4], which necessitates a shift toward **In-Situ Resource Utilization (ISRU)** to minimize logistics and launch costs [5]. Lunar regolith, the unconsolidated mineral layer covering the Moon's surface, has been identified as a critical feedstock for this purpose [6]. Much like terrestrial soil, lunar regolith is characterized by complex particle size, shape, and mineralogical distributions formed through millions of years of meteoritic weathering[7-9]. Recent research has confirmed the feasibility of consolidating this regolith into structural components, providing a foundational pathway for autonomous and economical lunar construction [10-13].

Various consolidation schemes, including sintering, concreting, and polymerization, have been investigated as viable methods for lunar regolith construction [12, 14-16]. The selection of a specific technique largely depends on its compatibility with autonomous systems, particularly Additive Manufacturing (AM) [17]. AM provides a critical strategic advantage: robotic systems can be deployed to the lunar surface in advance of human crews to independently prepare and construct habitats. However, identifying the optimal AM method requires extensive evaluation, as the highly variable particle sizes and the light-absorbent (dark) nature of lunar regolith can entirely preclude certain techniques [18-20]. In this work, we propose extrusion-based 3D printing as a robust solution that accommodates significant regolith particle size variation while utilizing a dual UV [21] and thermal curing process for complete consolidation [22]. Compared to alternatives such as vat photopolymerization, powder bed fusion, or directed energy deposition (DED), this extrusion-based approach is highly energy and resource-efficient, making it ideally suited for autonomous construction [23-27]. By combining AM with polymerization, this method facilitates the development of intricate structural designs while maximizing the use of local regolith as a primary building material.

Several Advancements have been made in using extrusion-based 3D printing of lunar regolith composites, with research exploring diverse binding materials and architectural designs. Initial efforts by Bao et al. [22, 28] explored the use of direct ink writing with epoxy resins to optimize slurry rheology for improved printing efficiency. Marnot et al. [26] and Ma et al. [27] subsequently evaluated the thermal durability of various polymer binders and the mechanical benefits of bio-inspired sandwich architectures in geopolymer composites under extreme lunar conditions. Some other researchers have explored thermoplastic binders, ranging from low-loading (**5–10 wt.%**) recyclable polylactide (PLA) to high-pressure extrusion systems using nylon powder that achieved up to **80 wt.%** regolith loading [23, 29]. Other innovations, such as the ARBURG Plastic Free forming (APF) technique for TPU-regolith composites and the development of specialized regolith simulant inks, have addressed common printing challenges like nozzle blockage and filament breakage [30-32]. Despite these advancements, future lunar missions face a critical dilemma regarding binder selection [33]. While thermoset matrices significantly enhance the mechanical functionality of 3D-printed parts, their permanent covalent bonds render them inherently insoluble, infusible, and impossible to recycle in resource-starved extraterrestrial environments. However, although recyclable thermoplastics offer sustainability, they often suffer from poor mechanical properties that limit their structural utility. To address this challenge, vitrimers have emerged as a promising material class by incorporating reversible covalent adaptable networks (CANs) [34, 35]. Vitrimers uniquely blend the mechanical resilience and thermal stability of thermosets with the recyclability and reprocessability of thermoplastics [36]. The adoption of vitrimer matrices in regolith composites offers a sustainable pathway for space applications, enabling long-term waste management and reduced construction costs through the continuous reuse of structural materials [37-39].

The self-healing and shape-memory performance of vitrimer composites relies heavily on the viscoelastic flow of the matrix and the reaction kinetics of the dynamic covalent networks and has been used in many fields including structural and non-structural applications [40, 41]. Therefore, this study isolates and prioritizes temperature, pressure, and time as the governing processing variables. Temperature serves as the primary driver for chain mobility; consistent with the **Williams-Landel-Ferry** (**WLF**) equation and Arrhenius relationships, heating the matrix above its glass transition temperature (**Tg**) reduces viscosity [42], allowing for the polymer chain diffusion necessary for interlayer bonding [43]. Pressure is equally critical for regolith-filled

systems to overcome surface roughness and ensure the physical wetting required for chemical exchange at the interface [44, 45]. Finally, these parameters were selected in lieu of environmental variables, such as humidity or atmospheric composition, to accurately simulate a lunar construction scenario where the 3D printing would occur in an arid vacuum, leaving thermal and mechanical inputs as the primary control mechanisms for efficient structural components.

Recent developments in 3D printing have led to the development of 4D printing, or printing structures that can alter their shape in reaction to outside stimuli [46]. Producing three-dimensional items that can transform into various three-dimensional structures when heated or cooled to a specific temperature or radiation is made possible by 4D printing, which uses shape-memory polymer in multi-material printing [47, 48]. Gyabaah et al. [49] reported 3D printing of regolith-filled shape memory vitrimer composite using LCD-based printing via vat-photopolymerization. However, there are some limitations as far as regolith weight percentage and printing size are concerned. In this study, we explored extrusion-based additive manufacturing of regolith-filled shape-memory vitrimer composite for lunar construction. A shape memory vitrimer regolith composite was synthesized using lunar regolith as the main constituent material and a recyclable, shape memory vitrimer (SMV) as the matrix of the composite. A relatively higher regolith weight percentage was used in the composite synthesis. The 3D-printed composite shows good thermomechanical properties, high self-healing efficiency, good shape memory properties, and excellent 3D-printable properties needed for lunar construction. To the best of our knowledge there is no prior work done like this in literature providing insight to the rheological, chemical and mechanical properties of the vitrimer-regolith composite for extraterrestrial applications.

2 Experimental

2.1 Materials and Methods

Bisphenol A glycerolate dimethacrylate and 1,4-butanediol dimethacrylate were obtained from Sigma Aldrich, USA. Ethyl (2,4,6-trimethylbenzoyl) phenylphosphinate was obtained from Oakwood Chemical, USA. Lunar Mare Simulant (LMS-1) regolith was purchased from The Exolith Lab. The materials were used as received.

2.2 Ink Synthesis and Characterization for Extrusion 3D Printing

Unlike previous works that rely on prefabricated thermoplastics or insoluble thermosets, this study introduces vitrimer as the binder for the lunar regolith simulant and successfully prints with a custom-built extrusion system. The approach supports high regolith loadings (up to 60 wt.%) and enables in-situ self-healing and shape recovery, which are not present in conventional lunar construction composites. The ink for the 3D printing comprises two major components: lunar regolith simulant and a shape memory vitrimer binder. The regolith simulant powder used for this project is Lunar Mare Simulant (LMS-1), which is located on the darker cratered regions of the Moon [45]. The simulant powder was used as received with no pretreatment. Recyclable SMV resin was prepared by mixing Bisphenol A glycerolate dimethacrylate (BPAGMA) as the monomer and Ethyl (2,4,6-trimethylbenzoyl) phenylphosphinate as the photoinitiator. Bisphenol A glycerolate dimethacrylate was heated at 110℃ for 1h. in an oven to reduce the viscosity for pouring. In this work, 3 % of the photo-initiator Ethyl (2,4,6-trimethylbenzoyl) phenyl phosphinate was dissolved in Bisphenol A glycerolate dimethacrylate (BPAGMA). 1,4-butanediol dimethacrylate diluent with varied weight percentage (10 wt.% and 20 wt.%) was added to the BPAGMA resin to control the viscosity of the ink to obtain the best extrudability. The mixture was stirred in a silicon oil bath at 120℃ for 3h. Different ink formulations consisting of two different regolith weight fractions (50 wt.% and 60 wt.%) were used in the ink preparation to determine the ink flow and best extrudability for 3D printing. **Table 1** below shows three different ink formulations for extrusion 3D printing.

Table 1. Composition of Three Different Slurry Formulations and the 3D Printed Composites

Ink Formulation	Composition of Binder	Regolith wt.%	Composite
A	Resin + 10wt.% Diluent	50	10D_50R
B	Resin + 10wt.% Diluent	60	10D_60R
C	Resin + 20wt.% Diluent	60	20D_60R

A custom extruder was assembled in our lab to study the 3D printability of the regolith vitrimer composite. An Ender-3 filament printer was modified into a slurry extrusion 3D printer.

The original filament print head was replaced by a custom high-viscosity extruder. The extruder is made of a barrel with a hopper as entrance for the composite slurry into the barrel and a stainless-steel screw rotated by a NEMA 23 stepper motor that converts the rotational motion of the screw into linear motion and eventually push the slurry down the extruder's body tube. Arduino Mega and a microstep controller are used to automate the printing process. The printing samples are modeled using SolidWorks software and imported into Cura slicing software and finally transferred to the 3D printer in STL format, as shown in **Scheme 1**. In this study, a print rate of **5mm/s** is used. A nozzle diameter of **10mm** is used, which also corresponds to the height of each printed layer. The UV-curable slurry ink is partially cured by a custom UV light with a wavelength of 365nm and an irradiation intensity of **40%** attached to the extrusion barrel while printing the photocurable slurry. The printing was done at room temperature. The printed sample was post-thermally cured in an oven for **3 hrs**. at **180 °C**. **Scheme 1** and **Figure 1** show the custom-made 3D printer, and several samples printed by this printer.

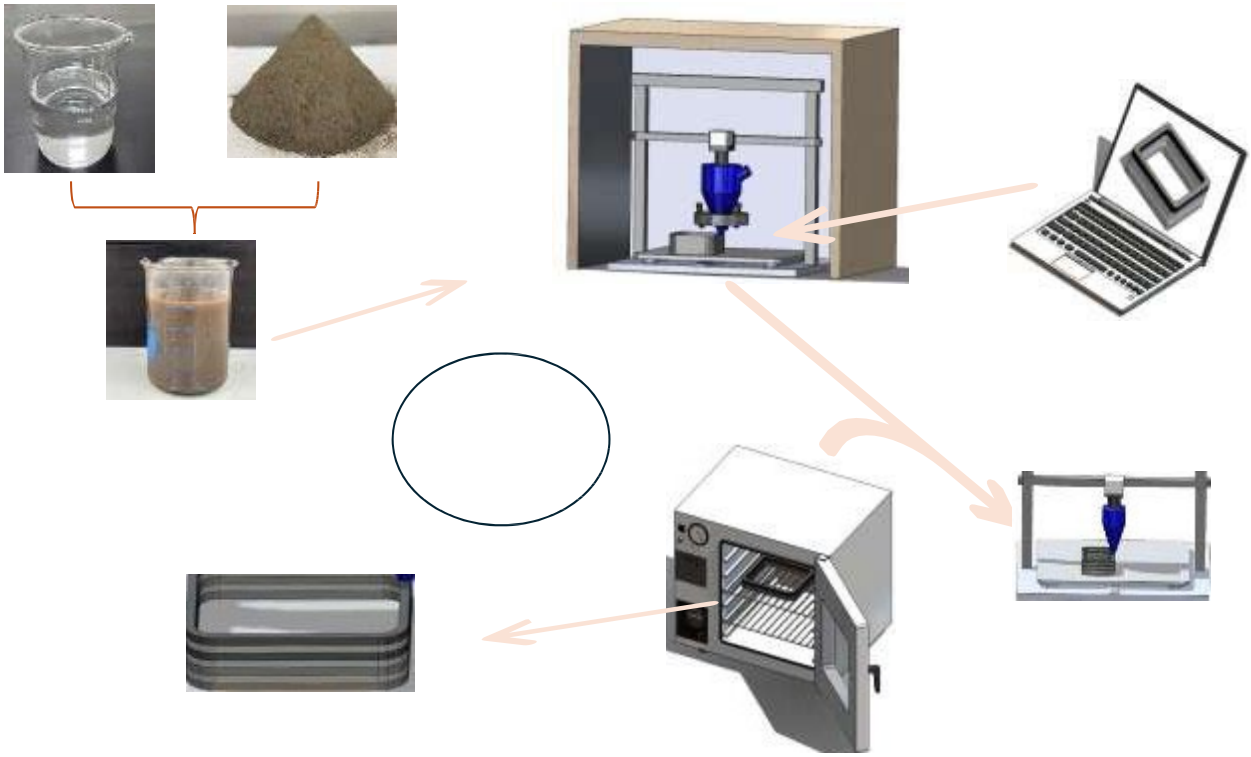

Scheme 1. Slurry Formulation and Extrusion 3D Printing

2.3 Materials Characterization

The viscoelastic properties of the polymer binder and the slurry used as the ink for 3D printing were determined using a Discovery HR 30 rotational rheometer from TA Instruments (New Castle, DE). The geometries of the test fixtures consisted of parallel disks with a diameter of 25 mm for all measurements. We performed thixotropic test on the neat and the various slurry compositions to determine how the slurry recovery rate. The test was done in 3 steps, a low-rate shear at 0.1 rad/s and a quick ramp to 100 rad/s and a sudden drop to 0.1 rad/s. A temperature sweep of the slurry was done at a heating rate of **5 ^{0}C/min** from **0 ^{0}C** to **100 ^{0}C** at a constant angular frequency of **10rad/s**. Both the conditioning time and sampling time were kept at **3s** for data acquisition.

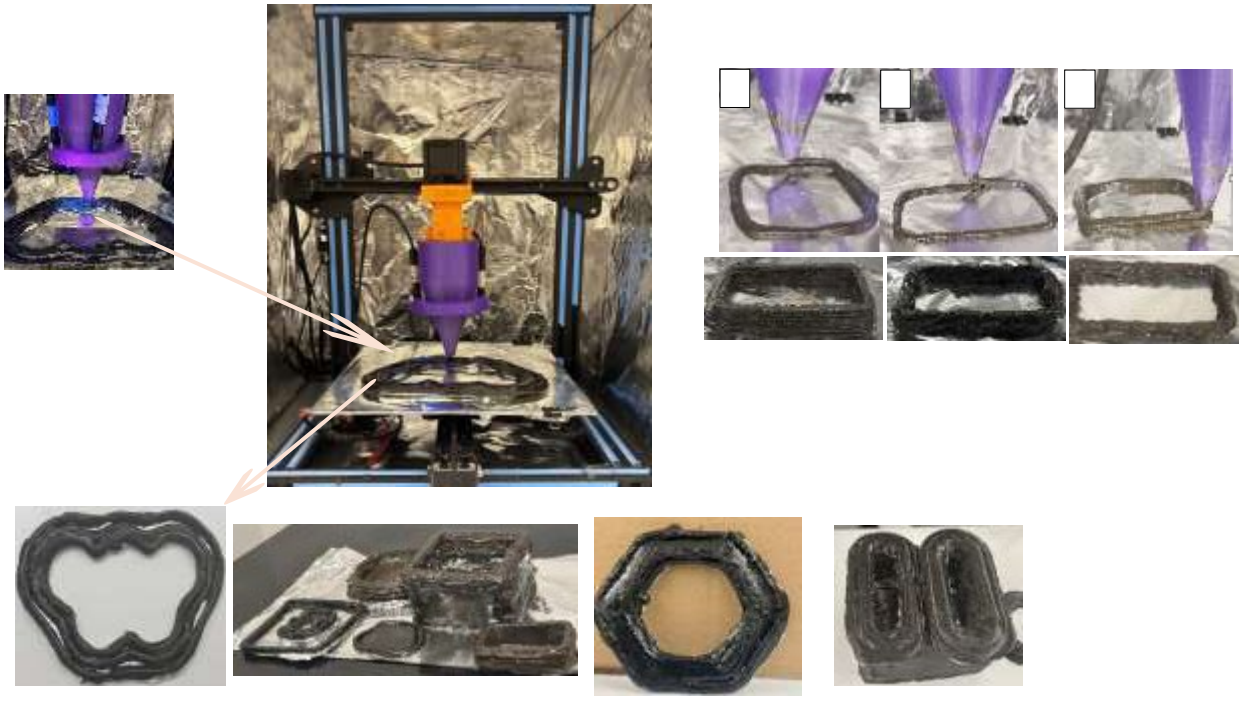

Figure 1. The modified homemade extrusion 3D printer, samples printed by the printer, and the extrudability and printability of the three types of composites.

All tests and characterizations perform used a minimum of 5 samples for each compositional formulation to ensure statistical reproduction and accuracy.

Perkin Elmer Spectrum Two Fourier Transfer Infrared Spectroscopy (**FTIR**) was utilized to determine the curing state of the 3D-printed samples after the post-thermal curing process. A total of 32 scans were collected with a scanning range of **4000cm^{-1}** to **400cm^{-1}** for both the ink sample and the 3D-printed composite.

The thermal stability, degradation temperature, and thermal decomposition of the 3D printed composites were examined using TGA550 thermogravimetric analysis (TGA) from 25 ℃.to 800 ℃ The weight loss and the derivative thermogravimetry (DTG) to temperature are plotted. To determine the glass and phase transition temperatures, we employed the PerkinElmer DSC 4000 was used to assess the regolith composite's response to heat flow. A mass of about 7-8 mg of the samples were used to perform the test. The temperature scan use **-10 ºC** to **200 ºC** at a rate of **10 ºC/min** and then held for **3 min**. It is then cooled from **200 ºC** to **-10 ºC** at the same rate and held for **5 mins,** which is considered as one full cycle for a run. Nitrogen gas flowing **20 mL/min** was used to feed the DSC chamber.

A thermomechanical programming cycle was used to quantify the shape memory behavior of the 3D-printed composite. A 3D printed cylindrical sample of known height (h_0) was placed between an MTS (QTEST 150) clamp fitted in an oven. The sample was heated at **140 °C** for **30 mins** to attain equilibrium. The sample at this temperature was compressed to a height of $\mathbf{h_1}$. After the compression, the load was maintained on the sample for **10 mins**, followed by rapid cooling to room temperature. The sample was taken out of the oven, and a new height of h_2 was taken. For shape recovery to occur, the sample was heated in a convection oven at **140 °C** for **20** mins and finally cooled to room temperature. The final height h_3 was recorded. The heights $\mathbf{h_0}$, $\mathbf{h_1}$, $\mathbf{h_2}$, and $\mathbf{h_3}$ were used to compute the shape fixity and shape recovery ratios.

2.4 Mechanical Characterization and Test for Healing Efficiency

The mechanical properties of the 3D printed composite were examined using uniaxial compression, low velocity impact, and 3-point bending tests. 3D printed cylindrical samples were polished for compressive testing. At least five effective samples of each composite were used for the compressive tests. The compressive behavior of the 3D printed composites was investigated at room temperature using an MTSQ150 machine with a **1 mm/min** loading rate. Rectangular specimens were printed for 3-point bending of the formulation with variations with dimensions of

170.56 mm × 25.4 mm × 5 mm seen in **Figure 2**. The span of the lower roller pins was maintained at **160m** to meet the ASTM D790 standard of length:thickness of **32:1**. Also rectangular specimen of dimension **152.40 mm × 25.40 mm × 5.08** mm was used for low velocity impact tests. Instron Dynatup 8250 HV impactor was used for the impact testing per **ASTM D3763-18**. At least 5 samples were used for the impact test, and the average value and standard deviation were recorded. From the impact test, the maximum impact load, crack initiation energy, and crack propagation energy were obtained.

An MTS Alliance RF/10 machine with a loading rate of **2 mm/min** was used to conduct the 3-point bending test. The flexural stress at the bottom surface of the mid-span was determined with **Equation 1**.

$$\sigma = \frac{3PL}{2bh^2} \quad (1)$$

where σ = flexural stress at the outer surface of the midspan, P = applied force, L = span length, b = beam width, and h = beam thickness.

Figure 2. 3D Printing of Horizontal Sample and Printed Sample under 3-Point Bending Test

The presence of covalent adaptable network (CANs) in the vitrimer matrix binder endows the composite with intrinsic properties such as self-healing and recycling properties[36, 50] . These matrix material properties are essential in a material-scarce environment like the Moon. In this project, 3D-printed rectangular samples **Error! Reference source not found.** were used for the self-healing test. Two successive healing cycles were performed after flexural tests. The healing was performed at **200 °C**, with a healing pressure of **10MPa** and a healing time of **4 hrs**, using the

Dakes Carver hot press. The second and third flexural tests were performed on the same samples after the healing. After the first flexural test, the 3D-printed composite was sandwiched between the Dakes Carver hot press at a temperature of **200 °C** for **4 hrs**. at a constant pressure of **10MPa** and then cooled to room temperature under the same pressure. Once at room temperature, the pressure was removed. The healing efficiency of the composite was calculated based on the flexural strength of two successive test cycles. **Equation 2** was used to compute the healing efficiency.

$$HE = \frac{F_H}{F_O} \quad \textbf{(2)}$$

where F_o and F_H represent the maximum flexural stress of the virgin and healed specimens, respectively.

All tests and characterizations are performed using a minimum of 5 samples for each compositional formulation to ensure statistical reproduction and accuracy.

3 Results and Discussions

3.1 Particle Size Distribution (PSD) of LMS-1

PSD analysis was done on the simulant using the Anton Paar PSA 1090 to understand the distribution of the particles as the largest particle sizes control the printing resolution and quantify the granulometric profile. Thus, this determines the complexity of designs possible without further treatment of the regolith. It assesses the impact on the extrusion-based 3D printing process. The PSD revealed a multimodal distribution with the mean particle size as seen in **Table 2** and **Figure 3**, **D_{50}** of approximately **140 µm** and a **D_{90}** value near **350 µm.** For this work, the nozzle orifice is about 10 mm when compared to the largest particle size **D_{90}** is about **28:1** which is also about **200%** more than the recommended threshold of **10:1** typically required to prevent mechanical "jamming" or clogging during the extrusion of high-viscosity mineral slurries. Consequently, the as-received LMS-1 simulant is well-suited for high-resolution autonomous construction without the need for energy-intensive sieving or grinding protocols on the lunar surface.

Table 2. A summary of particle size distribution of the as-received LMS-1

Run #	D_{10} (µM)	D_{50} (µM)	D_{90} (µM)	Mean Size (µM)	Span
1	25.84	140.63	350.19	171.98	2.31
2	25.01	139.05	349.17	170.89	2.33
3	25.90	143.74	361.01	176.04	2.33
4	25.89	145.08	362.65	176.98	2.32
5	25.28	140.77	356.74	173.51	2.35
6	27.63	150.49	367.88	181.00	2.26
7	26.59	148.21	367.89	179.77	2.30
Average	26.02	143.99	359.36	175.74	2.32

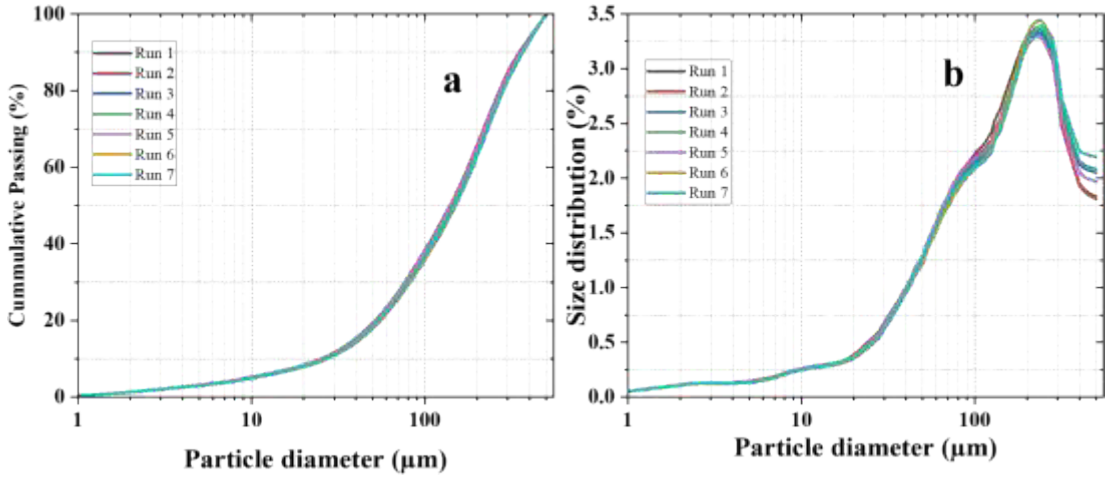

Figure 3. Particle size distribution run on the LMS-1 should the size variation of the regolith. a. S-curve of the cumulative passing of the particles. b. particle size distribution curve.

3.2 Rheology of the Slurry for 3D Printing

The study of the rheological properties of slurry shows the deformation and fluidity of the material under external stimuli, i.e. shear rate and temperature. This is to understand the correlation between the slurry and its compositions particularly the influence of the regolith content. In this work, we focused on the printability of the slurries composed of different regolith weight percentages and varied resin formulations. The effects of regolith ratio and fraction of diluent in the polymer formulation on the performance of the ink-slurry and the printing efficiency were

compared; see **Figure 4**. From the graph, both curves exhibit a rapid drop in viscosity as the temperature increases from **0 to 40 °C**. The increase in thermal energy led to a reduction in intermolecular interactions, which allowed the easy flow of the slurry. The polymer formulation with 20% diluent shows consistently lower viscosity in a wide temperature range compared to the 10% diluent. The increase in the diluent concentration dilutes the polymer matrix, leading to a reduction in the overall viscosity [51]. The viscosity plateaus beyond **40 °C**, indicating the lowest viscous state. A repeating series of sharp peaks was observed in the viscosity of the slurries at regular intervals. The peaks are superimposed on a slightly oscillating viscosity baseline. The higher peaks may be attributed to the presence of larger and coarser regolith particulates [52] . The irregularly shaped and different sizes of the particulate regolith in the slurry are responsible for the oscillations in the viscosity. Nevertheless, this peak in the viscosity did not affect the smooth flow of the slurry during the extrusion printing.

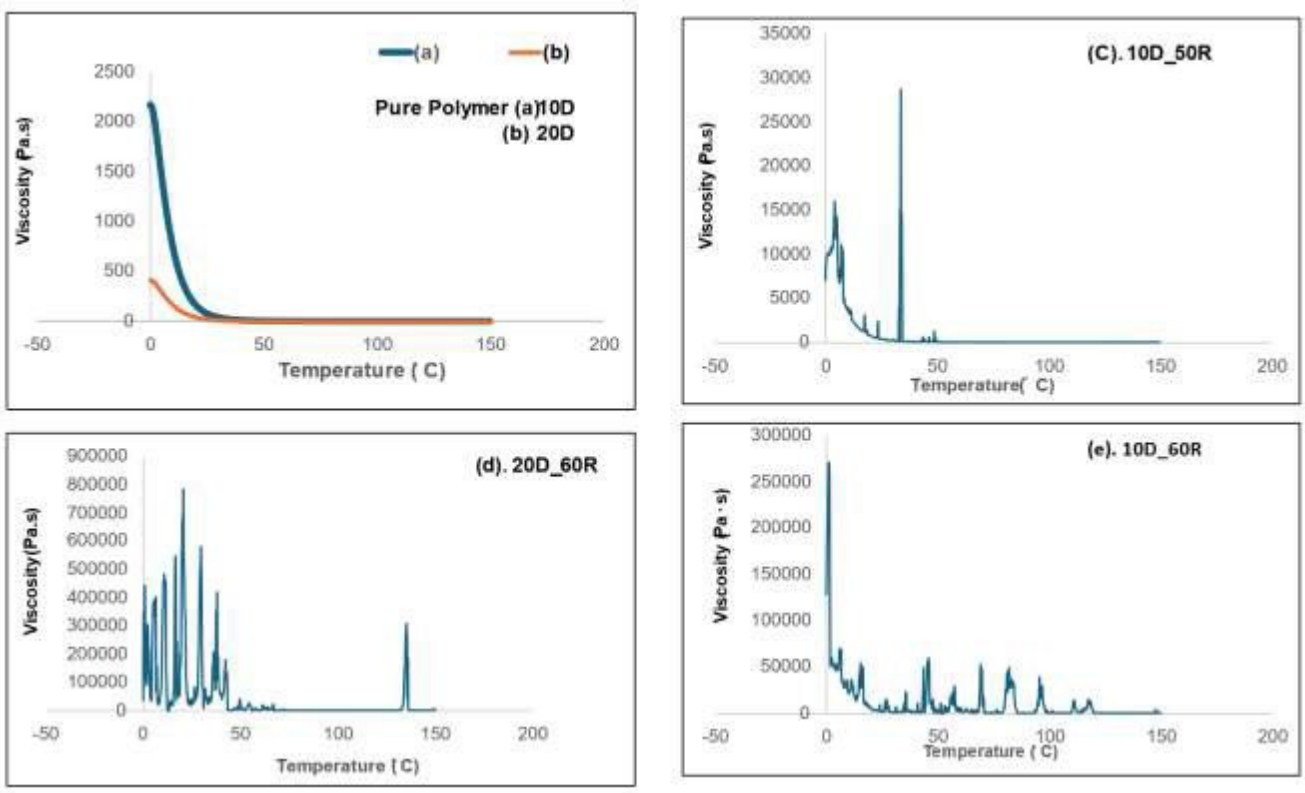

Figure 4. Change of Viscosity with Temperature of the pure polymer (a) 10D, (b) 20D, (C) 10D_50R, (d) 20D_60R, and (e) 10D_60R.

3.3 Thixotropic and Shear Stress Analysis

To understand and quantify the extrudability of the slurry, its necessary to conduct a yield and thixotropic analysis on the slurry. For thixotropy, the test simulates 3 stages during the extrusion. 1). When the slurry sits in the nozzle, it experiences low stress (shear rate of about **0.1 rad/s**). 2). The slurry as is pushed through the orifice at high stress rate, the slurry flows more easily possess (at rate of **100 rad/s**, significantly larger than the extrusion rate of **10 mm/s**). 3). A sudden reduction of the shear rate back to **0.1 rad/s** to simulate the slurry as it's printed into a shape. If the slurry moves from **step 2 to 3** and the shear moduli is greater or equal to the shear moduli in step 1, the slurry can be extruded, and it will maintain its shape. In **Figure 5**, the plot shows **step 1** (black) and **3** (blue). This plot combines storage (lower) and loss (higher) moduli, and the storage modulus of **step 3** is equal or greater than step 1. This means that during extrusion or printing at high rates, the slurry that is printed can keep its shape without deforming or flow.

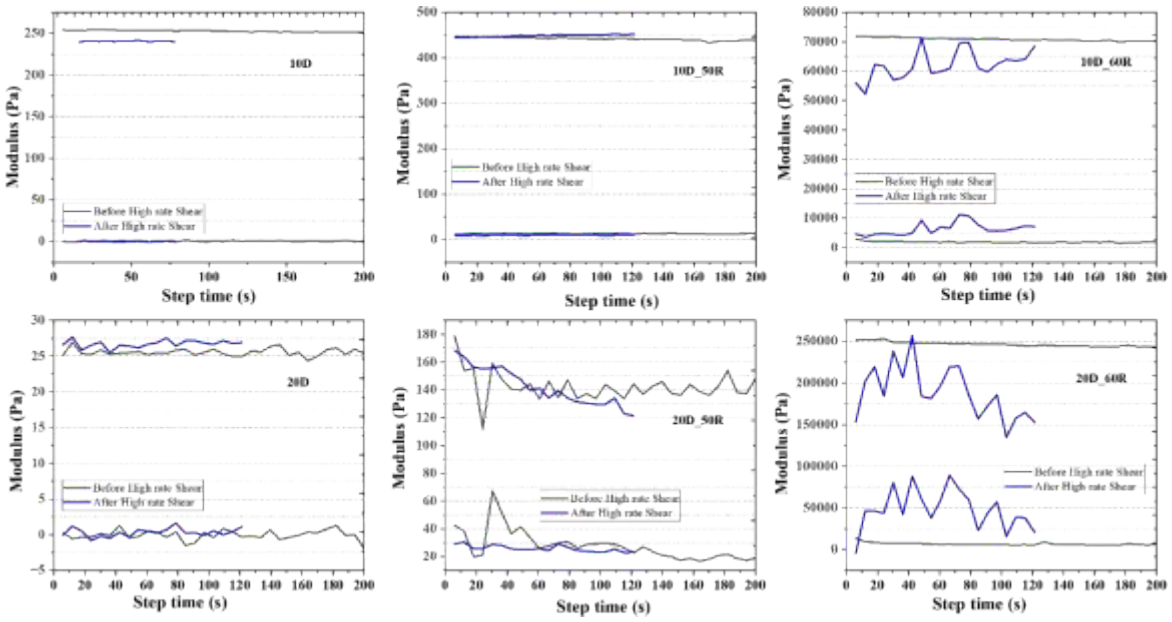

Figure 5. Thixotropic analysis of neat vitrimer and variation of slurry compositions

3.4 Bulkley -Herschel Yield Stress Analysis

Bulkley-Herschel Yield stress analysis was conducted to determine the maximum stress the slurry can withstand before collapsing. That is, the rheological behavior of the slurries was

modeled using the Herschel-Bulkley equation to quantify the yield stress y_0, which represents the critical stress threshold required to initiate flow.

This is to assess if a layer can support other layers, it has not been fully cured during the UV curing phase i.e. structural buildability of the composite, specifically determining the capacity of a freshly deposited. In **Figure 6**, the yield stress shows a positive correlation with regolith concentration. We believe the phenomenon is attributed to the presence of irregularly shaped, high-surface-area regolith particulates that function as physical crosslinks, effectively restricting the mobility of the polymer chains within the vitrimer matrix. However, the trend reverses which the diluent content is change. This is because the diluent, a low molecular methacrylate, acts like a lube increasing the free volume of the chains and allowing the chains to glide easily pass each other. This shows that the material in its slurry form may be able to withstand some few layers prior to full post thermal curing to improve the strength of the composite structure 3D printed.

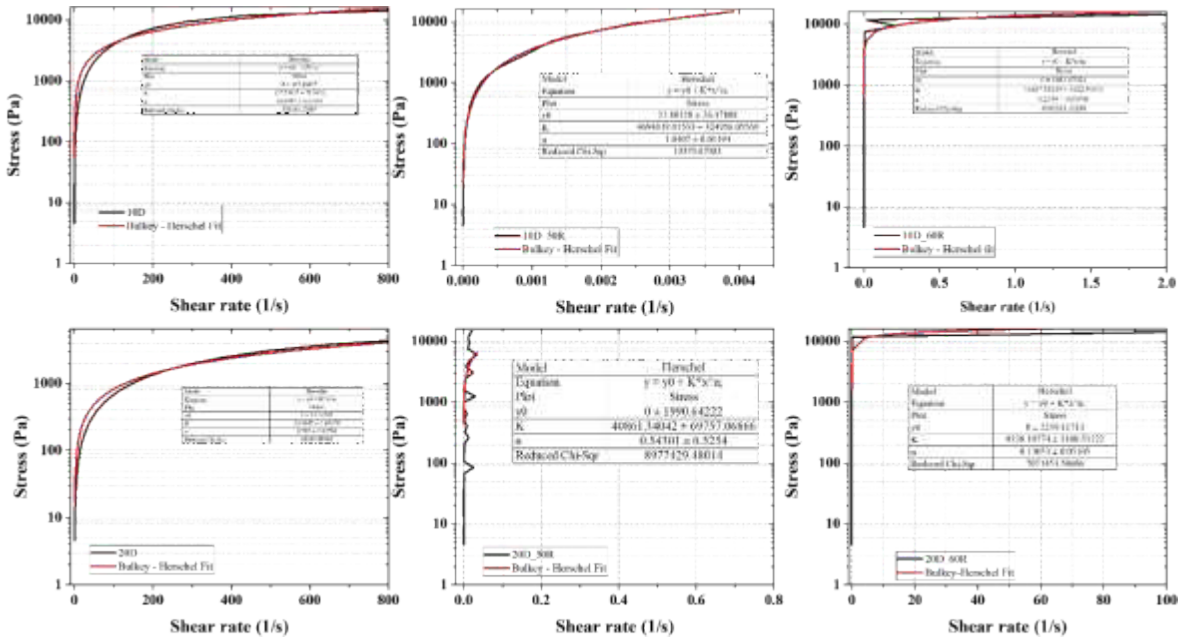

Figure 6. Bulkley- Herschel Yield Stress analysis on the neat vitrimer and regolith variations

3.5 FTIR and Chemical Characterization

FTIR was used to analyze the chemical transformations of the vitrimer-regolith slurry into a cured structural composite. The photoinitiated curing mechanism primarily involves free radical polymerization of the acrylate groups in the BPAGMA and BDDMA. The reaction is triggered by the homolytic cleavage of C-P bond upon UV irradiation to generate highly reactive benzoyl and phosphinoyl radicals, a **Norrish Type 1** decomposition. The radicals initiate the crosslinking transforming the vitrimer to a robust CAN. The significant changes in the characteristics transmittance peaks show the efficiency of the photoinitiated curing. A major focus of this study is the presence of **-OH functional groups**, which are pertinent to the catalyst-free **transesterification reactions** that govern the self-healing and shape-recovery properties of the regolith composite. In **Figure 7**, The band absorption at **3200 – 3600 cm^{-1}** which represents the -OH groups, exhibited a notable decrease in intensity in the cured slurry compared to the initial matrix. Such reduction can be attributed to the density increase of the network after curing. This limits the vibrational freedom of the chains lowering the detectable concentration of surface-active hydroxyl groups. Adding the LMS-1 regolith reduces the optical transmittance of the samples. This explains why the "cured slurry" spectrum transmittance remains consistently above **95%** primarily due to the scattering and absorption of the IR radiation by the dense dark regolith. This optical interference, combined with the complete breakdown of the aliphatic **C=C double bonds** near **1600 cm^{-1}** and **1638 cm^{-1}**, provides a definitive proof of the high conversion achieved through the dual UV and post-thermal curing cycles. The results confirm that while the regolith provides structural reinforcement, the vitrimer matrix maintains the chemical functionality required for autonomous repair in lunar environments.

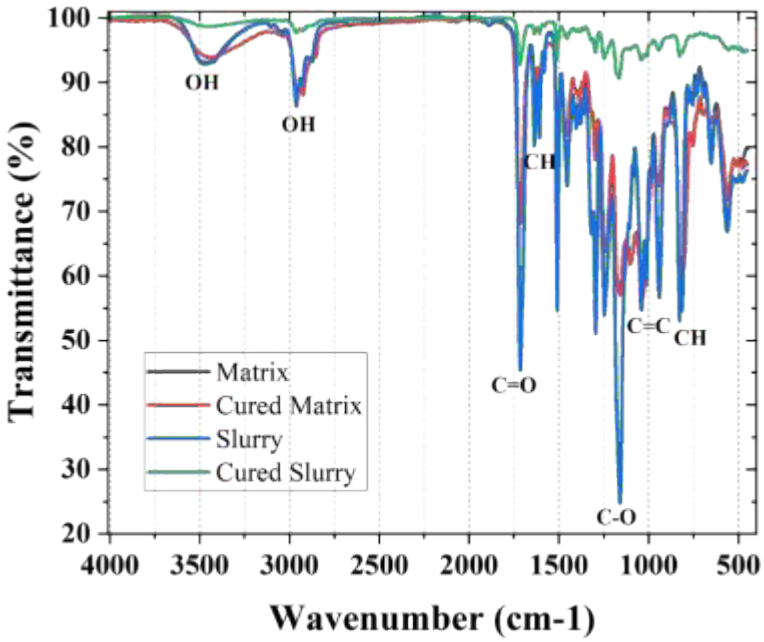

Figure 7. FTIR spectra analysis of neat vitrimer matrix and slurry for both cured and uncured variations

3.6 Mechanical Test Results

The mechanical performance of the 3D-printed composites was analyzed under uniaxial compression, low-velocity impact, and the 3-point bending tests. The 3D-printed composites from the 3 different slurry formulations exhibit similar responses under both compression and low velocity impact tests, with slight variations in mechanical properties. The **10D_50R** recorded the highest compressive strength; see **Figure 8d**. Increasing the regolith ratio in the slurry with **10 wt.%** diluent led to a slight decrease in the compressive strength. This may be due to the high porosity in the composite caused by the irregularly shaped particulate regolith as recorded by Gyabaah et al [49]. The **20D_60R** exhibits a relatively more ductile failure characterized by a higher energy absorption before fracture and a gradual rise in the clear peak of the impact load curve in **Figure 8a**. A brittle failure occurred in the **10D_60R** and **10D_50R** composite, as shown by the lower energy absorption and sudden drop in the impact load in **Figure 8b and 8c**, respectively. The higher impact resistance in the **20D_60R** also validates its high bending strength of **156.59MPa** in Error! Reference source not found.. Maximum crack propagation energy was

recorded in the composites with higher regolith concentration, which may be caused by the stress concentration at the polymer-regolith interface, causing matrix cracks and interfacial debonding, leading to higher crack propagation energy.

One of the major important parameters which is needed to evaluate the mechanical performance of composite is to understand its deformation behavior by observing the stress-strain curve during flexural 3-point bending test. In **Figure 9a**, all variations experienced a linear deformation followed by sudden failure. Narrowing **20D_60R** formulation, it reached a peak strength of about **156.45 ± 4.09 MPa** showing the high performance of the composite even with a high diluent content. We believe that the **60 wt%** regolith loading reached a critical percolating threshold where the mineral phase significantly contributed to the load-bearing capacity of the structure. Increasing the regolith in the series in **Figure 9b** increased the measured strength observed further corroborating that the regolith forms physical crosslinking nodes in the network restricting chain slip. **Table 3** summarizes the mechanical test results.

3.7 Thermal Characterization

Several thermal characterization tests were performed to determine the thermal properties and behavior of the regolith composite. Thermal stability test was performed using the Thermogravimetry analysis. TGA was performed from **25°C** to **800°C** to quantify the degradation profile and residue content of the varied formulations. All composites exhibited a highly similar, single-step decomposition behavior, indicating that the thermal degradation is primarily controlled by the vitrimer matrix rather than the inorganic lunar regolith as seen in **Figure 10a.** The onset of decomposition occurred at approximately **375°C**, with the maximum rate of mass loss T_{max} observed at **400°C**. This high thermal stability is critical, as it significantly exceeds the maximum lunar surface temperature of **130°C** published by NASA in 2025, ensuring structural components don't depolymerize during lunar daytime. In **Figure 10b**, the presence of a single peak in the DTG curves confirms that the diluent and BPAGMA monomer formed a homogeneous, well-integrated network without phase-separated degradation. As expected, the regolith phase remained stable up to **800°C**, and the final ash content for the **60 wt.%** samples matched the intended loading, providing a secondary quantitative verification of the composite composition.

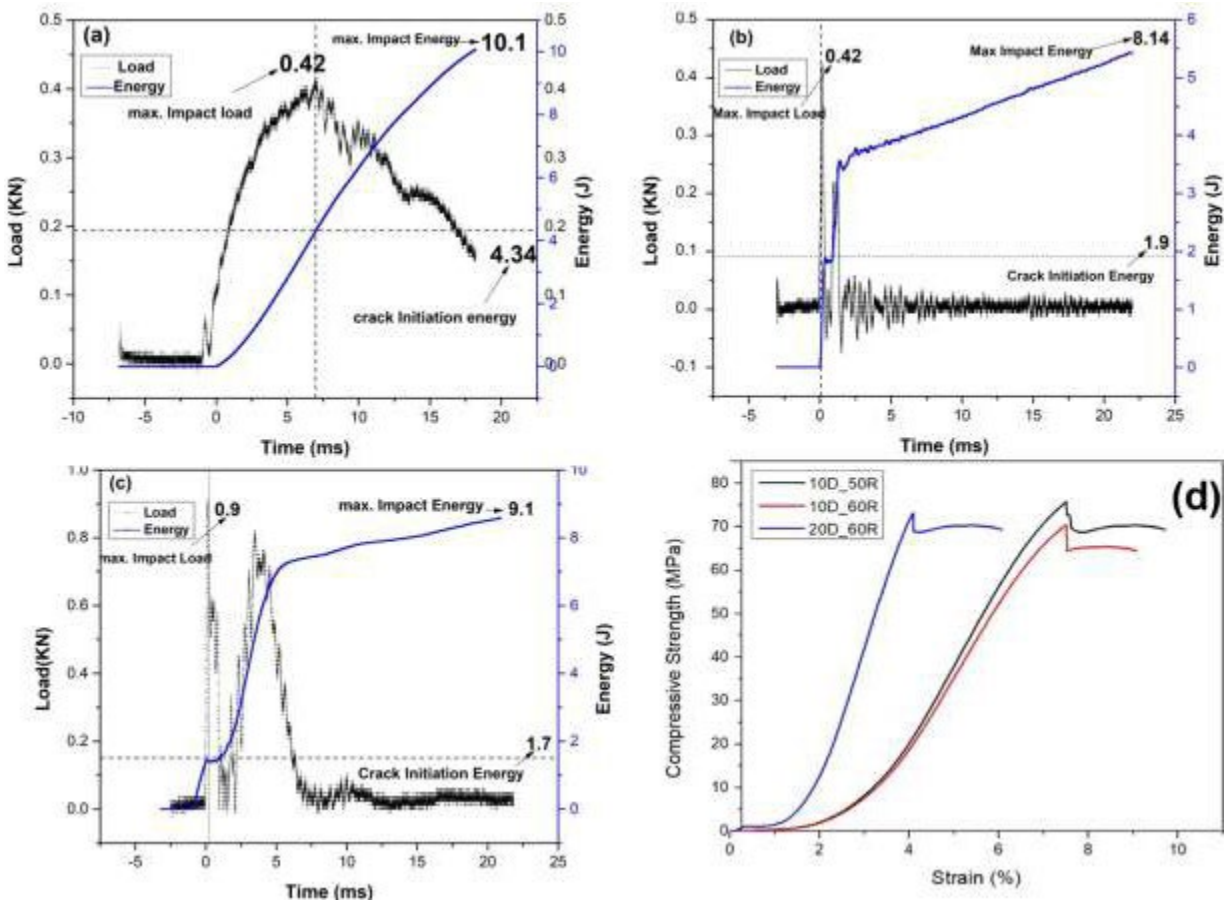

Figure 8. Graph of load and energy traces of low-velocity test: (a) 20D_60R, (b) 10D_60R, and (c) 10D_50R, and (d) compression stress-strain curves of the three types of samples at room temperature.

Table 3. Mechanical properties of 3D-printed composite based on uniaxial compression, three-point bending, and low-velocity impact tests.

Sample	Max. Impact Load (KN)	Initiation Energy(J)	Propagation Energy (J)	Flexural Strength (MPa)	Compressive Strength (MPa)
20D_60R	0.42 ± 0.02	4.34 ± 0.71	5.76 ± 0.86	156.59 ± 4.09	73.32 ± 1.09
10D_60R	0.756 ± 0.03	3.70 ± 0.90	5.41 ± 0.24	127.2 ± 4.71	70.40 ± 0.20
10D_50R	0.423 ± 0.22	3.63 ± 0.41	4.51 ± 0.59	118.4 ± 2.95	75.12 ± 2.01

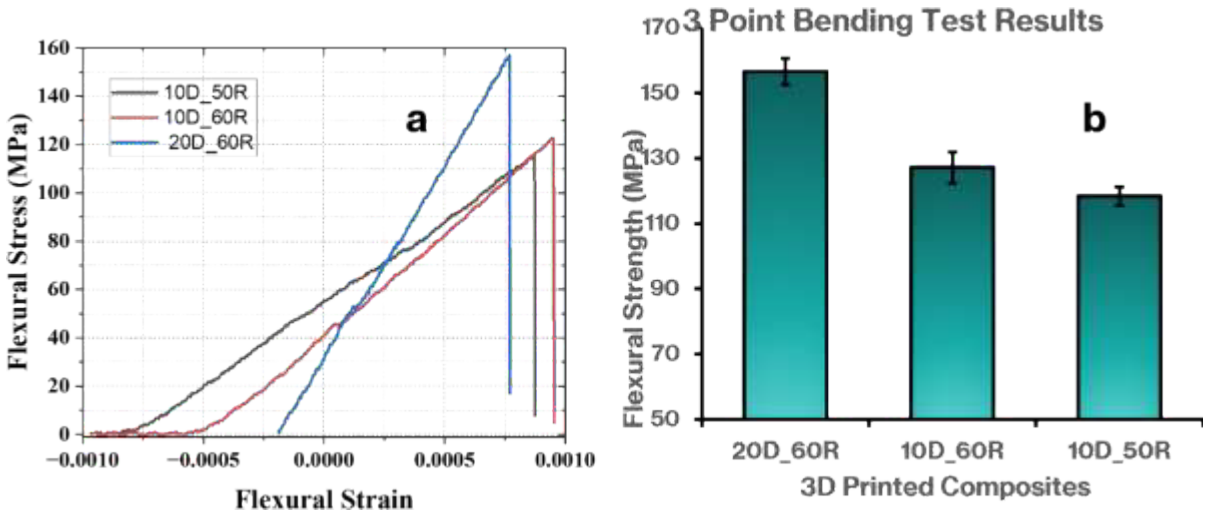

Figure 9. 3-point bonding of the various vitrimer composite formulations. a. Stress-Strain curve of composites. b. Bar plot showing distribution of measured properties

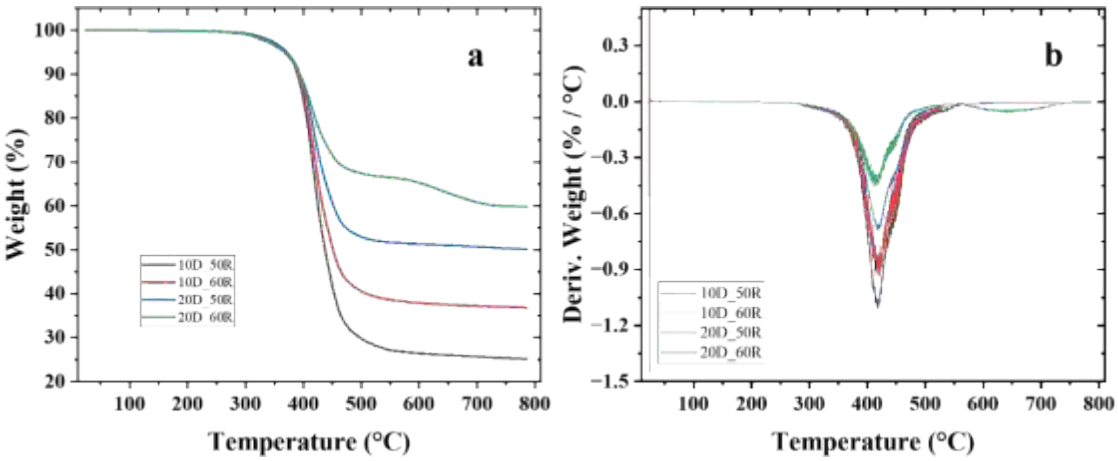

Figure 10. Thermogravimetry analysis of the lunar regolith composites. a. Thermal Stability plot. b. DTG plot

The Differential scanning calorimetry (DSC) test was used to determine the glass and phase transition temperature, $\mathbf{T_g}$, a crucial parameter for defining the *"service window"* of the composite. The results are given in **Table 4** and also shown in **Figure 11**. A consistent trend was observed where increasing the regolith content resulted in a significant increase in $\mathbf{T_g}$. For the 10 wt.%

diluent series, T_g rose from **147.95°C** for the pure vitrimer to **189.58°C** for the **60 wt.%** regolith formulation as seen in **Table 4**. This increase is attributed to the restricted mobility of the polymer chains at the high-surface-area regolith interface, indicating robust interfacial compatibility. Conversely, increasing the diluent concentration from **10 wt.%** to 20 wt.% led to a notable reduction in T_g. For example, the **20D_60R** sample exhibited a T_g of **183.67°C** compared to the **189.58°C** of the 10D_60R formulation. This validates the role of the diluent as a molecular lubricant that increases free volume and chain mobility. Crucially, all measured T_g values remain well above the **130°C** lunar peak temperature, ensuring that the structures will remain in a rigid, glassy state during operation to prevent premature softening or structural creep.

Table 4. A summary of the glass transition temperature of the various compositions of the regolith composite

Sample	T_g (°C)
10D	147.95 ± 2.3
10D_50R	181.13 ±2.9
10D_60R	189.58 ± 5.7
20D	141.85 ± 1.9
20D_50R	156.05 ± 3.2
20D_60R	183.67 ± 4.8

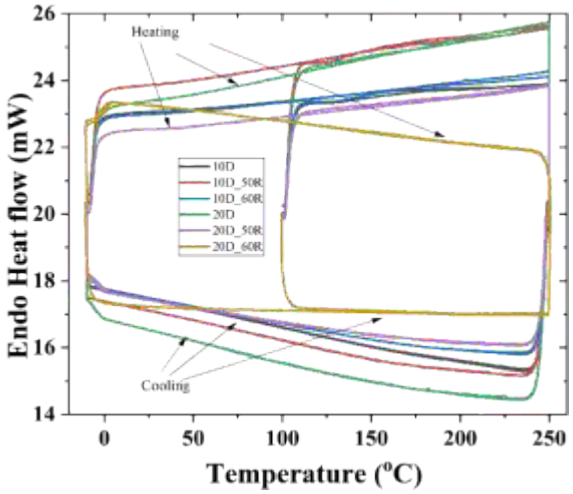

Figure 11. DSC test showing the Tg of the composite samples

The thermal performance of the prepared vitrimer-regolith composite is a significant advancement over traditional thermoplastic and thermoset binders which have been used in lunar construction research. While previous studies utilizing Polylactide (PLA) reinforced with low regolith loadings reported significant degradation and recycling challenges under thermal stress, the current vitrimer system achieves **60 wt.%** regolith loading while maintaining a $\mathbf{T_g}$ as high as **189.58°C**. Research on regolith-epoxy composites demonstrated excellent strength but lacked the reprocessability required for sustainable in-situ resource utilization (ISRU). Our vitrimer matrix bridges this gap by offering the mechanical resilience of a thermoset, with compressive strengths reaching **75 MPa**, alongside the intrinsic self-healing and recycling capabilities of a thermoplastic. By achieving $\mathbf{T_g}$ strategically above the maximum lunar surface temperature, this work ensures a stable operating window that surpasses typical epoxy or thermoplastic binders which may experience significant softening in extraterrestrial environments.

3.8 Temperature and Frequency Sweep Studies

As discussed in **Section 3.7**, the T_g increased with the regolith content. The crosslink density, ν_e, of the composite can be calculated using **Equation 3**.

$$E' = 3\nu_e RT \qquad (3)$$

where E' is the Elastic storage modulus, R, the gas constant and T, temperature at the rubbery plateau, typically estimated at $\mathbf{T_g + 40\ ^\circ C}$. According to the theory of rubber elasticity, the crosslink density of a polymer network is proportional to its storage modulus in the rubbery plateau region. The above equation provides quantifiable technique of measuring how the high-regolith loading influences the formation and integrity of the covalent adaptable network. In **Figure 12**, incorporating the lunar regolith significantly altered the apparent crosslink density of the system. For the **10 wt.%** diluent series, the calculated ν_e increased from the neat vitrimer baseline to the **60 wt.%** regolith composites. The increase in this is attributed to the fact that the irregular shapes of the regolith particles act as effective physical crosslinks, restricting the mobility of the vitrimer chains and reinforcing the structural network. However, for the **20D** series, the diluent acted as a molecular lubricant as stated earlier which facilitated the chains to slip past the regolith, reducing the elastic stiffness. Overall, it can be seen in **Figure 12** that the Elastic storage modulus increased with increasing regolith content [53].

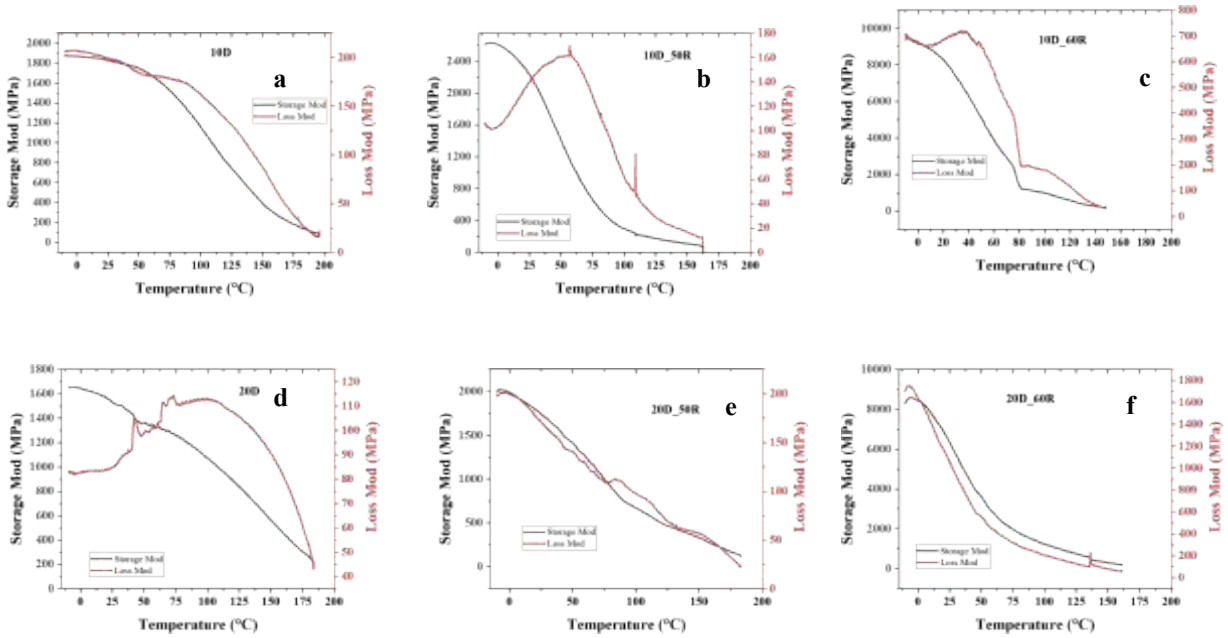

Figure 12. Temperature and frequency sweep at 1Hz using the DMA to evaluate the Elastic Storage and Loss Modulus, E' and E" respectively. (a) 10D, (b) 10D_50R, (c) 10D_60R, (d) 20D, (e) 20D_50R, and (f) 20D_60R.

3.9 Shape Memory and Self-Healing Properties of the 3D Printed Composites

Error! Reference source not found.**Figure 13** shows the heights of the composites at different stages of the compression programming-recovery cycle. The shape fixity ratios of the different composites **20D_60R,10D_60R**, and **10D_50R** were **83.90, 84.21**, and **90.02%**, respectively. A relatively lower shape recovery ratios of **79.09, 81.07**, and **83.46%**, respectively, were obtained for the **20D_60R,10D_60R**, and **10D_50R** samples, respectively. This is understandable because only the shape memory vitrimer matrix has shape memory effect; therefore, the higher the content of the vitrimer matrix in the composites, the better the shape memory effect [54]

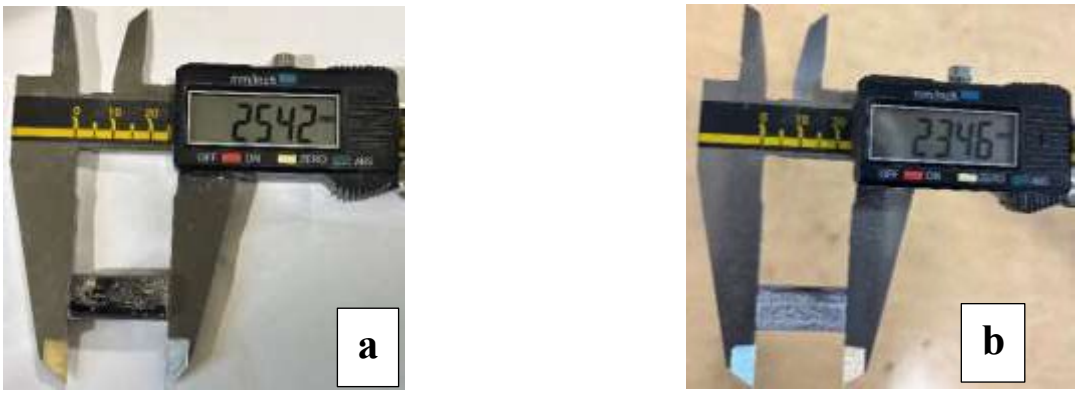

Figure 13. (a) The initial height of the specimen, (b) the height of the specimen after free shape recovery

In **Figure 14a**, we show the stress-strain-temperature relation during the programming of the vitrimer regolith. The ADMET MTS machine was used for this test where the oven was heated above **150 °C**, the $\mathbf{T_g}$ of the vitrimer. It can be seen that at this temperature the stress needed to compress and program the samples were lower compared to the room temperature compressive strengths. **Figure 14b** shows the stress recovery as a function of time. When conducting the stress recovery test, the temperature was fixed at 150°C.

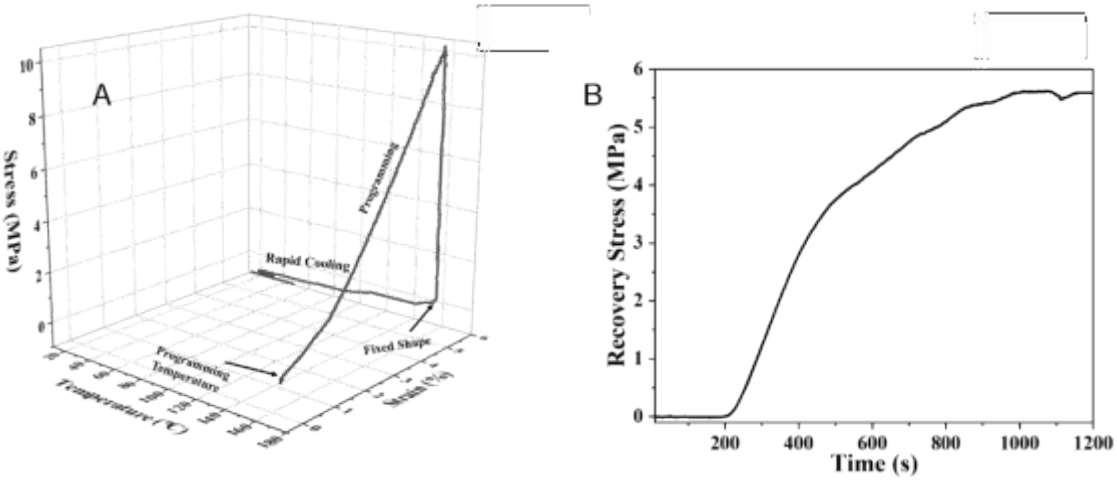

Figure 14. A typical thermomechanical programming procedure, including heating and loading, cooling (quick cooling followed by slow cooling), and unloading. a. Thermal Programming b. Stress recovery with time at a fixed temperature of 150 °C

The catalyst-free transesterification reaction of the vitrimer matrix in the rubbery state is responsible for the self-healing and the recovery of mechanical properties of the composites after any mechanical damage [36]. Visual inspection of the cracks and the recovery of the mechanical properties of the healed samples were used to calculate the healing efficiency of the composites after two different damage/healing cycles. **Error! Reference source not found.Figure 15 (a) and (c)** show some cracks in the composites after the first round of the flexural test, whereas **Figure 15 (b) and (d)** show a reduction in the crack size after the first healing cycle. **Table 5** summarizes the healing efficiencies from the first and second healing cycles. For most vitrimer, external catalysts are needed to accelerate the transesterification reaction process for the healing to take place. It is important to note, nevertheless, that in this study, the transesterification reaction in the vitrimer occurred without the addition of any exogenous catalyst. In situ, tertiary amines served as the internal activator in the vitrimer. This shows that the 3D-printed composite undergoes self-healing without the incorporation of other external healing agents.

While no quantification of surface roughness test was conducted, the applied healing pressure of **10 MPa** was sufficient to overcome interfacial surface asperities, ensuring the intimate contact required for the transesterification reaction across the fracture surfaces. The healing efficiency of **77.99%** achieved in this study (**10D_50R**) is notably high for a particle-filled composite system, particularly when compared to similar vitrimer-based studies. For instance, comparing to Tetteh et al. [39, 49] reported a healing efficiency lower compared to what we reported for our 10D_50R. Also, Mahoney, Tetteh [55] reported of **51.0%** for a similar vitrimer system healed under a lower pressure of **5 MPa**. The significantly higher efficiency observed here is attributed to the increased healing pressure (**10 MPa**), which effectively overcomes the surface asperities and yield stress of the high-viscosity regolith slurry, ensuring the intimate interfacial contact required for the transesterification reaction. Furthermore, while neat vitrimers can achieve near **100%** recovery, highly filled composites typically exhibit lower efficiencies (**30–65%**) due to the physical obstruction of polymer flow by the rigid fillers. Therefore, the ability of the **10D_50R** composite to retain nearly **78%** of its strength suggests that the **10 MPa** pressure was sufficient to facilitate adequate matrix flow and bond exchange despite the **50 wt.%** solid regolith loading. Comparing the mechanical and thermal performance of the developed vitrimer-regolith composite represents a significant advancement over traditional binders utilized in extraterrestrial construction research. For instance, PLA-regolith composites [23] only achieved moderate loading

and faced challenges with thermal degradation, the current system achieves a **60 wt.% loading** and a high $\mathbf{T_g}$ value of almost **190 °C**. The results were also benchmarked against a nylon and epoxy based systems [26, 29], which revealed that the vitrimer matrix provided a unique combination of high flexural strength **156.59 MPa** and the ability to retain **69.12%** of its mechanical integrity after multiple failure-healing cycles. The dual functional of high strength and reprocessabilty makes this vitrimer-regolith a superior candidate for long-term autonomous lunar construction compared to conventional thermoplastic or non-recyclable thermoset binders [54].

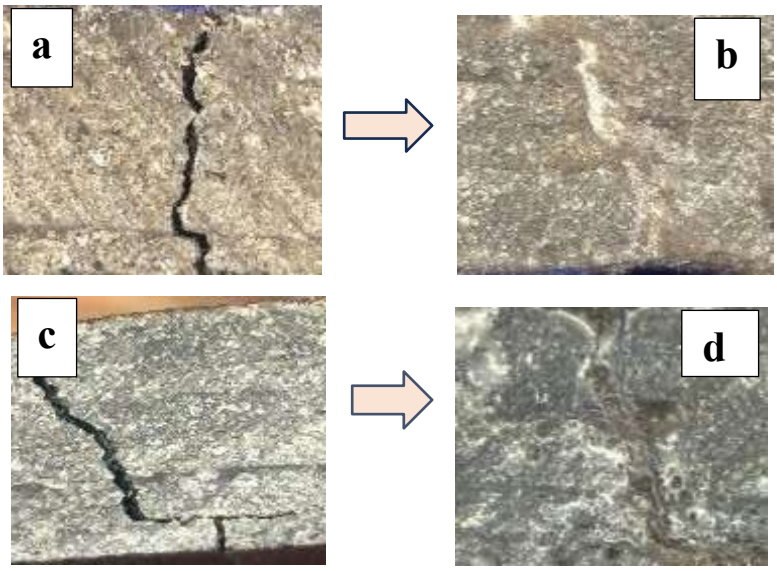

Figure 15. Cracked Specimens (a and c) and healed specimens (b and d).

Table 5. Healing Efficiency and Shape Memory Properties of 3D-Printed Composites.

Sample	Healing Cycle	Healing Efficiency	Shape Fixity Ratio (%)	Shape Recovery Ratio (%)
20D_60R	1	67.67 ± 1.21	83.90 ± 0.21	79.09 ± 0.09
	2	57.92 ± 1.93		
10D_60R	1	68.88 ± 2.22	84.21 ± 0.70	81.07 ± 1.20
	2	59.04 ± 1.15		
10D_50R	1	77.99 ± 1.70	90.02 ± 0.20	83.46 ± 1.90
	2	69.12 ± 0.24		

3.10 SEM and Morphological Analysis

We used the JSM-6610 LV SEM chamber to observe the surface of two variations of the samples, which are **10D_50R** and **20D_50R**, from the DMA failure samples to briefly explore and explain the nature of the failure. Prior to the SEM image, a thin conductive coat was applied to the surface of the specimen in a suitable holder to prevent localized charging.

The SEM micrographs provide important morphological evidence of the energy dissipation mechanisms during mechanical failure. Both compositions exhibited highly irregular and textured fracture surfaces, which are characteristic of **ductile failure** in polymer composites. Rather than the smooth and shape, surfaces typical of brittle cleavage, these samples show significant plastic deformations and localized yielding of the vitrimer matrix. The high surface roughness indicated that advancing crack fronts were repeatedly deflected and pinned by the dispersed lunar regolith particulates, forcing a tortuous fracture path that required higher energy to propagate.

Comparing the micrographs reveals that the **Figure 16b 20D_50R** formulation exhibits more pronounced plastic flow and "tearing" features compared to the **Figure 16b 10D_50R** sample. This morphological difference is directly correlated with the higher diluent concentration, which functions as a molecular lubricant, as discussed in previous sections, to increase chain mobility and decrease the overall network crosslink density. Furthermore, the micrographs show a cohesive interface between the large, spherical regolith particles and the vitrimer binder, with no significant evidence of large-scale debonding. This robust interfacial adhesion ensures effective stress transfer from the polymer to the mineral phase, ultimately contributing to the superior flexural and compressive strengths observed in these 3D-printed structural components.

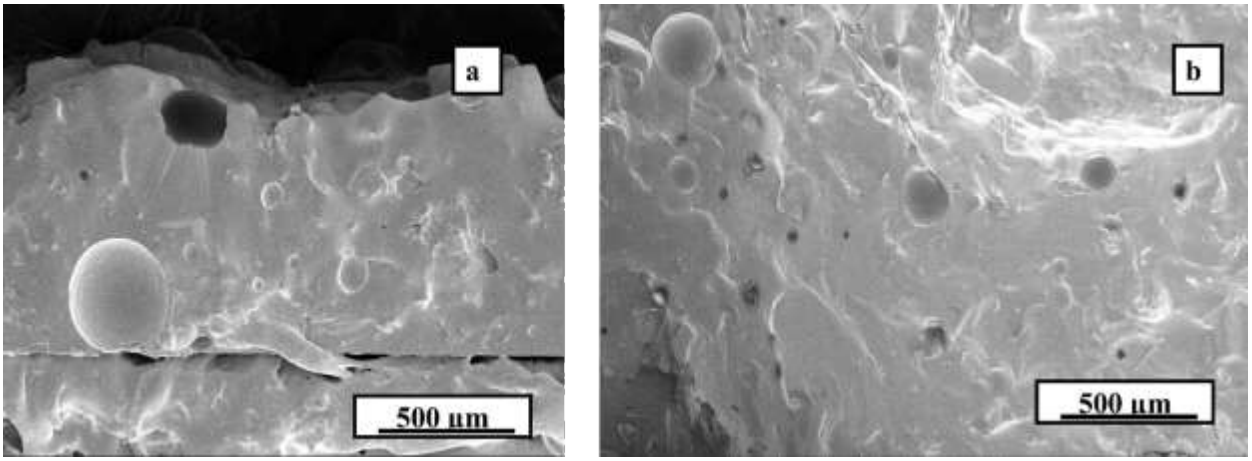

Figure 16. SEM micrograph showing fracture surface of samples from DMA. (a) 10D_50R, and (b) 20D_50R.

4 Conclusion

The design and development of this shape-memory and self-healing vitrimer-regolith composite represents a significant advancement in the field of **ISRU** for autonomous extraterrestrial construction. By studying and integrating chemical, thermal, mechanical and rheological analyses, this study demonstrates a material system capable of meeting the rigorous structural and environmental demands of extraterrestrial habitats. **FTIR** characterization confirmed that the UV-initiated **Norrish Type I** photoinitiation successfully crosslinks the dimethacrylate matrix, while keeping the essential **-OH** and **C=O** functional groups required for dynamic transesterification and the formation of **CANs.** This robust chemical network allows the material to transition from a processable slurry to a structural solid that retains intrinsic self-healing capabilities. Analyzing the rheological properties, the Herschel-Bulkley and thixotropic analyses prove that the **60 wt.%** regolith compositional formulations possessed the ideal "printability window.". The high yield **($y_0 \approx 2500$ Pa)** and rapid structural recovery after high shear rates scientifically justify the successful extrusion of **10 mm** layers without structural collapse or slumping. The stability is further enhanced by the frequency independent **E'** determined in the DMA sweeps, indicating a stable, percolating network of regolith particulates within the binder. **Thermomechanical evaluations** revealed that the regolith composite's T_g and thermal stability significantly exceeded the extreme **130 °C** lunar surface temperature report by NASA. With T_g values as high as **189.58°C** and thermal decomposition onsetting at **375 °C,** the structure remained

in a rigid, glassy state during the lunar day, preventing premature softening or creep. Furthermore, the calculated crosslink density highlighted how the **60%** filler loading acted as an effective physical reinforcement, resulting in a flexural modulus of approximately **8.5 GPa**. The morphological analysis via SEM confirms a ductile failure mode with robust interfacial adhesion between the vitrimer and the lunar simulant (LMS-1). These combined findings provide a comprehensive scientific foundation for using high-loading vitrimer composites as a sustainable, reprocessable, and resilient medium for building the next generation of lunar infrastructure. Ultimately, the mechanical testing proved that composites are capable of withstanding medium to high strength applications and capable of self-healing upon damage due to CANs available.

Acknowledgement

This work is supported by the NASA Cooperative agreement NASA (2024-25)-Rapid-MGT-12, US National Science Foundation under grant number OIA-1946231, and the Louisiana Board of Regents for the Louisiana Materials Design Alliance (LAMDA), and US National Science Foundation under grant number OIA-2418415.

Data Availability Statement

The datasets generated during and/or analyzed during the current study are available from the corresponding author on reasonable request.

Author Statement:

KYG: Conceptualization, Methodology, Analysis, and Writing-Original Manuscript; ON: Conceptualization, Methodology, Analysis, Writing-Original Manuscript, and Data Curation; BM: Data Curation; MJ: Supervising, Writing-Revising; PM: Supervising, Funding, Writing-Editing; BS: Funding, Writing-Editing; EJ: Funding, Writing-Editing; GL: Conceptualization, Supervising, Funding, Writing-Editing and Revising.

Declaration of Conflicts of Interests

The authors of this work have declared no conflicts of interest.

References

1. Smith, M., et al., *The Artemis Program: An Overview of NASA's Activities to Return Humans to the Moon.* IEEE Aerospace Conference Proceedings, 2020: p. 1-10.
2. Zhang, P., et al., *Overview of the Lunar In Situ Resource Utilization Techniques for Future Lunar Missions.* Space: Science and Technology (United States), 2023. **3**: p. 1-18.
3. Lu, W., et al., *Mechanical properties of short-age CQU-1 lunar regolith simulant geopolymer for in-Situ resource utilization.* Construction and Building Materials, 2025. **492**: p. 143072.
4. Just, G.H., et al., *Parametric review of existing regolith excavation techniques for lunar In Situ Resource Utilisation (ISRU) and recommendations for future excavation experiments.* Planetary and Space Science, 2020. **180**: p. 104746.
5. Xu, Q., P. Hollingsworth, and K. Smith, *Launch cost analysis and optimization based on analysis of space system characteristics.* Transactions of the Japan Society for Aeronautical and Space Sciences, 2019. **62**(4): p. 175-183.
6. Labeaga-Martínez, N., et al., *Additive manufacturing for a Moon village.* Procedia Manufacturing, 2017. **13**: p. 794-801.
7. Noble, S.K., L.P. Keller, and C.M. Pieters, *Evidence of space weathering in regolith breccias I: Lunar regolith breccias.* Meteoritics & Planetary Science, 2005. **40**(3): p. 397-408.
8. Noble, S.K., L.P. Keller, and C.M. Pieters, *Evidence of space weathering in regolith breccias II: Asteroidal regolith breccias.* Meteoritics & Planetary Science, 2010. **45**(12): p. 2007-2015.
9. McKay, D.S., et al., *The lunar regolith.* Lunar sourcebook, 1991. **567**: p. 285-356.
10. Zhang, T., et al., *Thermal vacuum regolith environment simulator for China's deep lunar drilling exploration.* Applied Thermal Engineering, 2018. **144**: p. 779-787.
11. Suescun-Florez, E., et al., *Geotechnical Properties of BP-1 Lunar Regolith Simulant.* Journal of Aerospace Engineering, 2015. **28**(5): p. 1-9.
12. Chen, M., et al., *Construction of a virtual lunar environment platform.* International Journal of Digital Earth, 2013. **6**(5): p. 469-482.
13. Chen, Y., et al., *An overview on lunar regolith simulants solidification methods: integrating chemical, physical, and MICP strategies for extraterrestrial construction.* Biogeotechnics, 2025: p. 100212.
14. Dou, R., et al., *Sintering of lunar regolith structures fabricated via digital light processing.* Ceramics International, 2019. **45**(14): p. 17210-17215.
15. Grugel, R.N. and H. Toutanji, *Sulfur "concrete" for lunar applications–Sublimation concerns.* Advances in Space Research, 2008. **41**(1): p. 103-112.
16. Toutanji, H.A., S. Evans, and R.N. Grugel, *Performance of lunar sulfur concrete in lunar environments.* Construction and Building Materials, 2012. **29**: p. 444-448.
17. Zocca, A., et al., *Enabling the 3D printing of metal components in μ-gravity.* Advanced Materials Technologies, 2019. **4**(10): p. 1900506.
18. Goulas, A., et al., *Assessing extraterrestrial regolith material simulants for in-situ resource utilisation based 3D printing.* Applied Materials Today, 2017. **6**: p. 54-61.
19. Chow, B.J., et al., *Direct Formation of Structural Components Using a Martian Soil Simulant.* Scientific Reports, 2017. **7**(1): p. 1-8.

20. Balla, V.K., et al., *First demonstration on direct laser fabrication of lunar regolith parts.* Rapid Prototyping Journal, 2012. **18**(6): p. 451-457.
21. Liu, M., et al., *Digital light processing of lunar regolith structures with high mechanical properties.* Ceramics International, 2019. **45**(5): p. 5829-5836.
22. Bao, C., et al., *3D printing of regolith-based epoxy composites with excellent temperature resistance and mechanical strength.* Acta Astronautica, 2025. **229**: p. 787-803.
23. Li, H., et al., *3D printing and solvent dissolution recycling of polylactide–lunar regolith composites by material extrusion approach.* Polymers, 2020. **12**(8): p. 1724.
24. Wang, Y., et al., *In-situ utilization of regolith resource and future exploration of additive manufacturing for lunar/martian habitats: A review.* Applied Clay Science, 2022. **229**: p. 106673.
25. Giovanni, C., et al., *Regolith-Rich PEEK Composite Bricks : Steps Towards Space- Ready Lunar Construction Materials.* Applied Thermal Engineering, 2025. **15**(2): p. 0-19.
26. Marnot, A., et al., *Thermal weathering of 3D-printed lunar regolith simulant composites.* ACS Applied Engineering Materials, 2024. **2**(8): p. 2016-2026.
27. Ma, S., et al., *3D-printed Lunar regolith simulant-based geopolymer composites with bio-inspired sandwich architectures.* Journal of Advanced Ceramics, 2023. **12**(3): p. 510-525.
28. Bao, C., et al., *Preparation and characterization of elevated and cryogenic temperature-resistant regolith-based epoxy resin composites.* Construction and Building Materials, 2023. **387**(April): p. 131560-131560.
29. Zhao, H., et al., *Development of lunar regolith-based composite for in - situ 3D printing via high-pressure extrusion system.* Acta Astronautica, 2023. **18**(2): p. 430-450.
30. Fateri, M., et al., *3D printing of flexible parts out of lunar regolith simulant.* Acta Astronautica, 2025. **229**: p. 779-786.
31. Fateri, M., et al., *Localized Microwave Thermal Posttreatment of Sintered Samples of Lunar Simulant.* Acta Astronautica, 2019. **32**(4): p. 1-7.
32. Cesaretti, G., et al., *Building components for an outpost on the Lunar soil by means of a novel 3D printing technology.* Acta Astronautica, 2014. **93**: p. 430-450.
33. Jakus, A.E., et al., *Robust and elastic lunar and martian structures from 3D-printed regolith inks.* Scientific Reports, 2017. **7**(1): p. 44931.
34. Utekar, S., et al., *Comprehensive study of recycling of thermosetting polymer composites–Driving force, challenges and methods.* Composites Part B: Engineering, 2021. **207**: p. 108596.
35. Krishnakumar, B., et al., *Vitrimers: Associative dynamic covalent adaptive networks in thermoset polymers.* Chemical Engineering Journal, 2020. **385**: p. 123820.
36. Alabiso, W. and S. Schlögl, *The impact of vitrimers on the industry of the future: Chemistry, properties and sustainable forward-looking applications.* Polymers, 2020. **12**(8): p. 1660.
37. Zhang, Y., et al., *Recent advances in recyclable thermosets and thermoset composites based on covalent adaptable networks.* Journal of Materials Science and Technology, 2021. **92**: p. 75-87.
38. Wu, Y., Y. Wei, and Y. Ji, *Carbon material/vitrimer composites: Towards sustainable, functional, and high-performance crosslinked polymeric materials.* Giant, 2023. **13**: p. 100136.
39. Tetteh, O., P. Mensah, and G. Li, *Repeated healing of low velocity impact induced damage in orthogrid-stiffened sandwich panel.* Journal of Composite Materials, 2023. **57**(23): p. 3619-3632.

40. Jin, Z., et al., *Self-recoverable, stretchable, and sensitive wearable sensors based on ternary semi-interpenetrating ionic hydrogels.* ACS Applied Polymer Materials, 2021. **3**(5): p. 2732-2741.
41. Han, F., et al., *High-Conductivity, Self-Healing, and Adhesive Ionic Hydrogels for Health Monitoring and Human-Machine Interactions Under Extreme Cold Conditions.* Advanced Science, 2025. **12**(16): p. 2412726.
42. Williams, M.L., R.F. Landel, and J.D. Ferry, *The temperature dependence of relaxation mechanisms in amorphous polymers and other glass-forming liquids.* Journal of the American Chemical Society, 1955. **77**(14): p. 3701-3707.
43. Montarnal, D., et al., *Silica-like malleable materials from permanent organic networks.* Science, 2011. **334**(6058): p. 965-968.
44. Kim, Y.H. and R.P. Wool, *A theory of healing at a polymer-polymer interface.* Macromolecules, 1983. **16**(7): p. 1115-1120.
45. Wool, R. and K. O'connor, *A theory crack healing in polymers.* Journal of Applied Physics, 1981. **52**(10): p. 5953-5963.
46. Alghamdi, S.S., et al., *Additive manufacturing of polymer materials: Progress, promise and challenges.* Polymers, 2021. **13**(5): p. 1-39.
47. Tibbits, S., *4D Printing.* Architect. Des, 2020. **84**: p. 421-433.
48. Ge, Q., et al., *Active origami by 4D printing.* Smart Materials and Structures, 2014. **23**(9): p. 094007.
49. Gyabaah, K.Y., et al., *3D printable regolith filled shape memory vitrimer composite for extraterrestrial application.* Journal of Composite Materials, 2024. **58**(24): p. 2639-2654.
50. Zhang, Y., et al., *Journal of Materials Science & Technology Recent advances in recyclable thermosets and thermoset composites based on covalent adaptable networks.* Journal of Materials Science & Technology, 2021. **92**: p. 75-87.
51. Denissen, W., et al., *Chemical control of the viscoelastic properties of vinylogous urethane vitrimers.* Nature Communications, 2017. **8**(1): p. 14857.
52. Suescun-Florez, E., et al., *Geotechnical properties of BP-1 lunar regolith simulant.* Journal of Aerospace Engineering, 2015. **28**(5): p. 04014124.
53. Li, G., Y. Zhao, and S.S. Pang, *Analytical modeling of particle size and cluster effects on particulate-filled composite.* Materials Science and Engineering: A, 1999. **271**(1-2): p. 43-52.
54. Li, A., A. Challapalli, and G. Li, *4D printing of recyclable lightweight architectures using high recovery stress shape memory polymer.* Scientific Reports, 2019. **9**(1): p. 7621.
55. Mahoney, B., et al., *Effect of Healing Parameters on the Healing Efficiency of A Vitrimer.* Journal of Applied Polymer Science, 2025. **142**(46): p. e57810.